

Article

DFT Study of Methylene Blue Adsorption on ZnTiO₃ and TiO₂ Surfaces (101)

Ximena Jaramillo-Fierro ^{1,2,*} , Luis Fernando Capa ³, Francesc Medina ¹  and Silvia González ²

¹ Departamento d'Enginyeria Química, Universitat Rovira i Virgili, Av Països Catalans, 2643007 Tarragona, Spain; francesc.medina@urv.cat

² Departamento de Química y Ciencias Exactas, Universidad Técnica Particular de Loja, San Cayetano Alto, 1101608 Loja, Ecuador; sgonzalez@utpl.edu.ec

³ Maestría en Química Aplicada, Universidad Técnica Particular de Loja, San Cayetano Alto, 1101608 Loja, Ecuador; lfcapa@utpl.edu.ec

* Correspondence: xvjaramillo@utpl.edu.ec; Tel.: +593-7-3701444

Abstract: The search for alternative materials with high dye adsorption capacity, such as methylene blue (MB), remains the focus of current studies. This computational study focuses on oxides ZnTiO₃ and TiO₂ (anatase phase) and on their adsorptive properties. Computational calculations based on DFT methods were performed using the Vienna Ab initio Simulation Package (VASP) code to study the electronic properties of these oxides. The bandgap energy values calculated by the Hubbard *U* (GGA + *U*) method for ZnTiO₃ and TiO₂ were 3.17 and 3.21 eV, respectively, which are consistent with the experimental data. The most favorable orientation of the MB adsorbed on the surface (101) of both oxides is semi-perpendicular. Stronger adsorption was observed on the ZnTiO₃ surface (−282.05 kJ/mol) than on TiO₂ (−10.95 kJ/mol). Anchoring of the MB molecule on both surfaces was carried out by means of two protons in a bidentate chelating (BC) adsorption model. The high adsorption energy of the MB dye on the ZnTiO₃ surface shows the potential value of using this mixed oxide as a dye adsorbent for several technological and environmental applications.

Keywords: DFT; ZnTiO₃; TiO₂; methylene blue; adsorption



Citation: Jaramillo-Fierro, X.; Capa, L.F.; Medina, F.; González, S. DFT Study of Methylene Blue Adsorption on ZnTiO₃ and TiO₂ Surfaces (101). *Molecules* **2021**, *26*, 3780. <https://doi.org/10.3390/molecules26133780>

Academic Editor:
Monika Wawrzekiewicz

Received: 25 May 2021
Accepted: 19 June 2021
Published: 22 June 2021

Publisher's Note: MDPI stays neutral with regard to jurisdictional claims in published maps and institutional affiliations.



Copyright: © 2021 by the authors. Licensee MDPI, Basel, Switzerland. This article is an open access article distributed under the terms and conditions of the Creative Commons Attribution (CC BY) license (<https://creativecommons.org/licenses/by/4.0/>).

1. Introduction

Over the past decade, Ti- and Zn-based oxides have received much attention due to their competitive cost, non-toxicity, excellent stability, availability, and ability to produce highly oxidizing radicals [1–4]. Titanium oxide (TiO₂) and zinc oxide (ZnO) are two well-known semiconductors that have been widely used to construct electron transport channels due to their appropriate bandgaps, efficient electron mobilities, and simple synthesis methods [5–8]. In addition, these oxides are promising semiconductors to eliminate organic pollutants with incomparable efficiency due to their tunable surface and structural functionality [9]. The ZnO–TiO₂ composite system has even more superior properties than the individual oxides due to the high separation rate of photogenerated carriers and the wide optical response range [10]. Several syntheses and characterization studies of the ZnO–TiO₂ system have shown that there are three compounds in this binary system, including ZnTiO₃ (cubic, hexagonal), Zn₂TiO₄ (cubic, tetragonal), and Zn₃Ti₃O₈ (cubic) [11–13].

ZnTiO₃ has many similar physical properties to TiO₂ and ZnO, including high electron mobility [14–16]. This ternary oxide has been widely used because of its outstanding properties and potential scientific and technical applications [17]. ZnTiO₃ has been investigated in a variety of applications as an antibacterial, catalyst, nanofiber, white pigment, microwave dielectric, gas sensor, nonlinear optical, corrosion inhibitor, and luminescent material [18–23], but its application in adsorption has not been sufficiently studied, despite the fact that the literature indicates that due to its great specific area, it could have an important potential as an adsorbent [24,25].

ZnTiO₃ is a polar oxide of the LiNbO₃-type (LN-type) with both cations coordinated octahedrally in a three-dimensional framework of the octahedron perovskite (Pv) that shares corners [26]. In this structure, both cations move along the trigonal axis *c*, thus producing a spontaneous polarization reinforced by a second-order Jahn–Teller (SOJT) distortion due to Ti⁴⁺ (d⁰) [27]. The paraelectric parent structure of ZnTiO₃ is the ilmenite (II)-type phase (hexagonal space group *R*-3), which is the stable phase under ambient conditions [28]. The crystalline and phase transformation behaviors of ZnTiO₃ have systematically been investigated by various authors regarding several synthesis methods, Ti:Zn precursor molar ratios, and calcination temperatures [29–35]. Furthermore, the literature agrees that obtaining ZnTiO₃ as a pure phase at a low processing temperature is a challenge in materials chemistry [36–38].

In a previous experimental paper, we reported the synthesis and characterization of the ZnTiO₃/TiO₂ nanocomposite. This heterostructure was indexed to a hexagonal phase with space group *R*-3(148) for ZnTiO₃ and a tetragonal phase with space group *I*4₁/amd(141) for TiO₂ (anatase) [39,40]. In these studies, we also reported the ability of ZnTiO₃/TiO₂ to remove the methylene blue (MB) dye in aqueous systems, and it was contrasted with the results obtained for pure TiO₂ (anatase). The results showed that the heterostructure has better photocatalytic adsorption and degradation capacity than anatase alone, probably due to a synergistic effect. This synergistic effect between semiconductors has been extensively studied, showing that the presence of a second semiconductor can provide special active sites to enhance the adsorption and photocatalysis of various compounds [41].

Although several properties of ZnTiO₃ have been extensively studied experimentally, a proper description of its electronic, optical, and adsorptive properties remains an active research area from a theoretical point of view [42] since, up to date, this ternary oxide has scarcely been studied with quantum methods [43]. Therefore, the computational study of the molecular interaction between ZnTiO₃ and methylene blue could contribute to clarifying the adsorption and degradation mechanism of this dye, favoring the development of materials for the treatment of waters contaminated with MB.

The elimination of MB in wastewater is an extremely important task in environmental protection because it has caused serious contamination in many countries of the world [44]. Methylene blue, known as methylthioninium chloride is a basic cationic dye widely used in the printing, plastics, paper, leather, food, pharmaceutical, and textile industries [45–47]. The discharge of wastewater effluents from these industries, with a high content of MB without efficient degradation, results in harmful effects for humans and animals [48].

Various technologies have been used to treat wastewater contaminated with dyes [49]. Among these techniques, adsorption is easy to perform without pretreatment and is highly selective for removing dyes [50]. In addition, adsorption has been found to be superior to other techniques for wastewater treatment in terms of initial cost, simplicity of design, ease of operation, and insensitivity to toxic substances [24]. Although there are several experimental studies of MB adsorption on different surfaces, some uncertainties remain due to lack of understanding at the molecular level of the MB adsorption mechanism on the ZnTiO₃ surface.

As is well known, computational calculations of the electronic structure in an isolated molecule can achieve the desired chemical precision as long as a sufficiently large basis set is used, the electronic correlation is sufficiently described, and the relativistic effects in the calculation are adequately included [51]. Therefore, in this study, Density Functional Theory (DFT) computational calculations were used to characterize the electronic structure of ZnTiO₃ and TiO₂ (anatase) and also to investigate the feasibility of using both oxides as MB adsorbents. The results presented in this paper clarify the previously obtained experimental results and confirm that ZnTiO₃ is an excellent adsorbent and that it has high potential for future technological and environmental applications.

2. Results

2.1. Optimization and Electronic Structure of ZnTiO₃ and TiO₂

The adsorption of the methylene blue molecule on the surface of both ZnTiO₃ and TiO₂ was modeled using the following parameters: hexagonal ZnTiO₃ with a cell = 5.148 Å × 5.148 Å × 13.937 Å <90° × 90° × 120°> and tetragonal TiO₂ with a cell = 3.821 Å × 3.821 Å × 9.697 Å <90° × 90° × 90°>, as shown in Figure 1. The coordinates of the optimized ZnTiO₃ and TiO₂ structures are detailed in Table S1 and the corresponding optimization energy values are included in Figure S2.

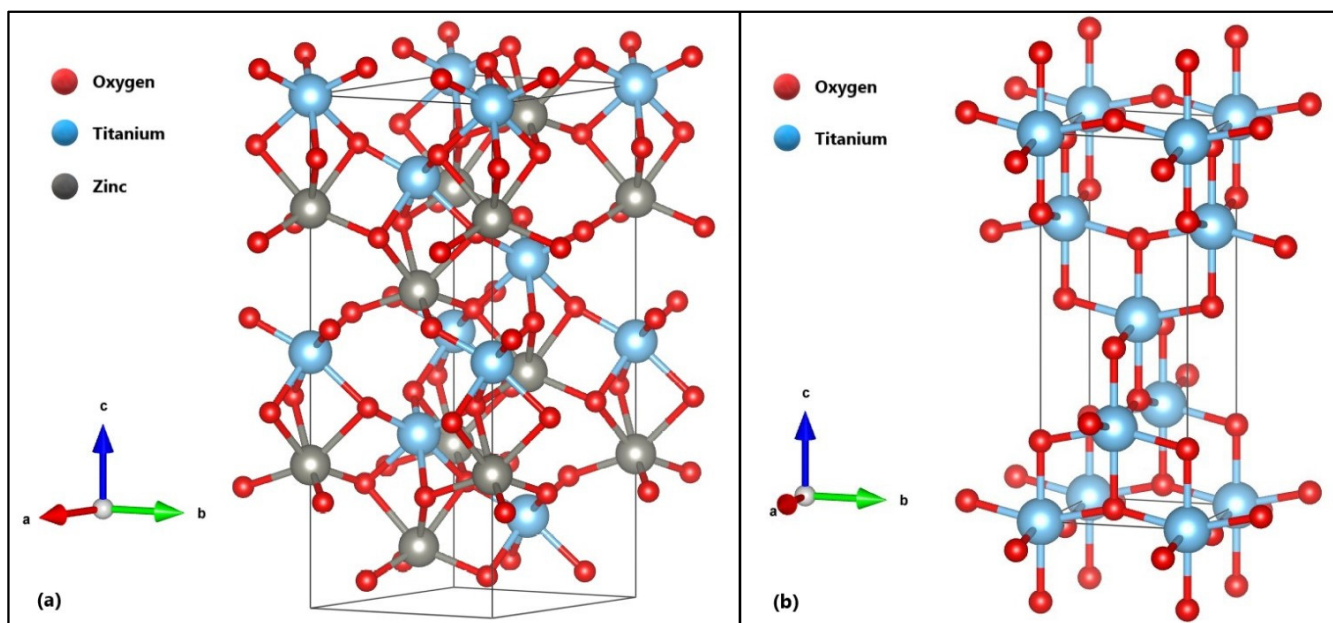


Figure 1. Optimized structures of (a) ZnTiO₃ and (b) TiO₂.

The selection of the high symmetry points and lines in the first Brillouin zone [52] and the results of the calculation of the electronic band structure of ZnTiO₃ and TiO₂ are shown in Figure 2a,b, respectively.

Figure 2a,b show that the indirect bandgap energy values of the ZnTiO₃ and TiO₂ structures calculated by the exchange–correlation functional in the generalized gradient approximation (GGA-PBE) method were 2.20 and 2.31 eV, respectively. However, the indirect bandgap values were also calculated by the GGA + U method, that is, incorporating the Hubbard *U* approximation term. Indirect bandgap calculations using GGA + U resulted in 3.16 eV (*U* = 2.5) and 3.21 eV (*U* = 4.0) for ZnTiO₃ and TiO₂, respectively. These results are in good agreement with the experimental results reported in the literature: 3.18 eV for ZnTiO₃ [15] and 3.20 eV for TiO₂ [53].

The total and partial density of states (DOS) of ZnTiO₃ and TiO₂ are illustrated in Figures 3 and 4, respectively. Figure 3a shows that the total density of state (TDOS) of ZnTiO₃ has two main zones: an upper conduction band (CB) zone from 2.5 to 6.2 eV, and a lower valence band (VB) zone, from −6.0 to −0.2 eV. The CB is dominated by the contribution of Ti, while the VB is dominated by the contribution of Zn and O. Figure 3b–d show the partial density of state (PDOS) of ZnTiO₃. As can be seen in Figure 3b, the main contribution of Ti in the CB is through the 3*d* orbital. On the other hand, Figure 3c shows that Zn contributes mainly to the VB through the 3*d* orbital while O interacts with Zn in this band through the 2*p* orbital shown in Figure 3d.

Likewise, Figure 4a shows that the total density of state (TDOS) of TiO₂ has two main zones: an upper conduction band (CB) zone from −0.1 to 3.8 eV, and a lower valence band (VB) zone, from −7.6 to −2.8 eV. The CB is dominated by the contribution of Ti, while the VB is dominated by the contribution of O. Figure 4b,c show the partial density of state

(PDOS) of TiO_2 . As can be seen in Figure 4b, the main contribution of Ti in the CB is through the $3d$ orbital. On the other hand, Figure 4c shows that O contributes mainly to the VB through the $2p$ orbital.

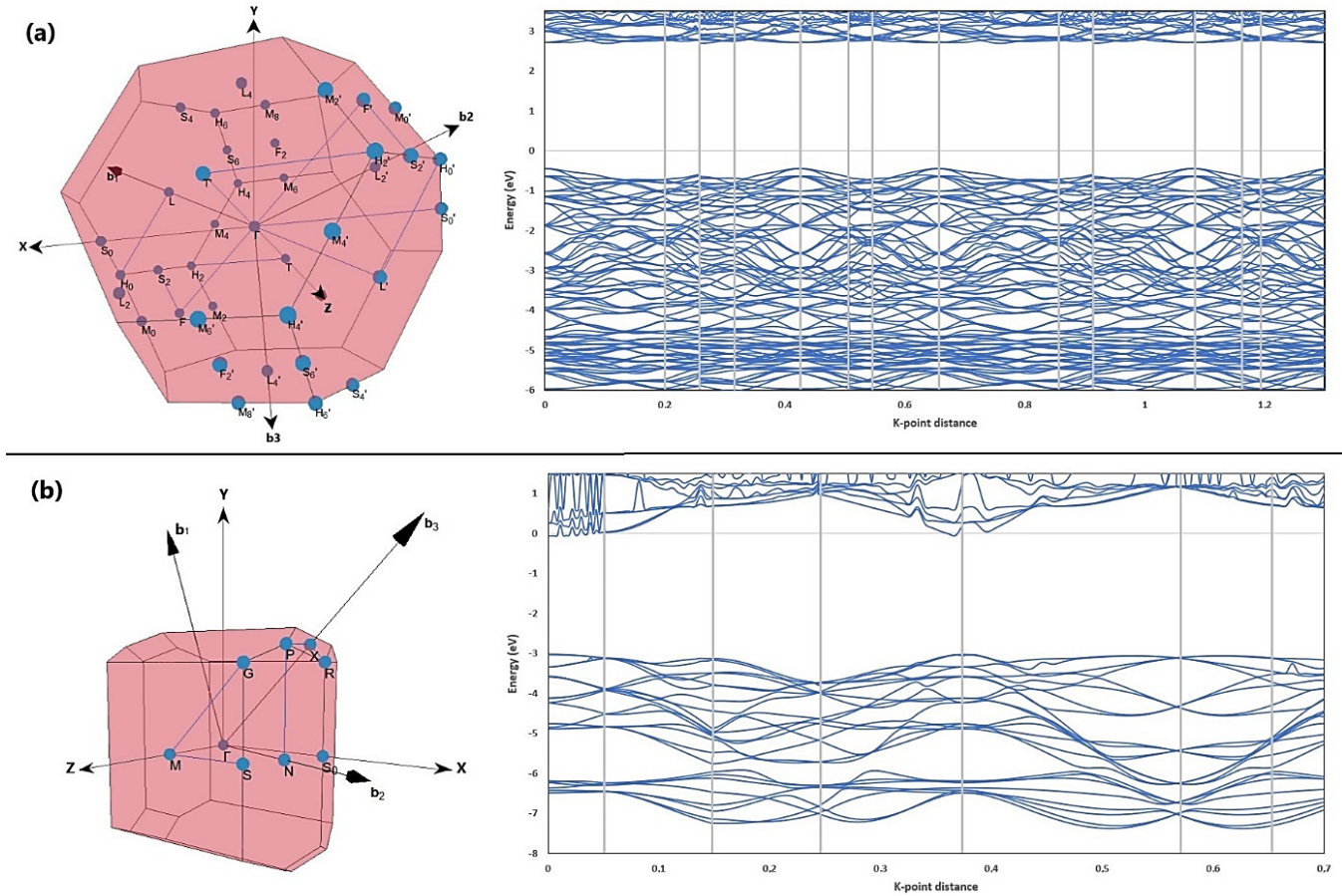


Figure 2. Band structures of (a) ZnTiO_3 and (b) TiO_2 along the high symmetry directions in the Brillouin zone.

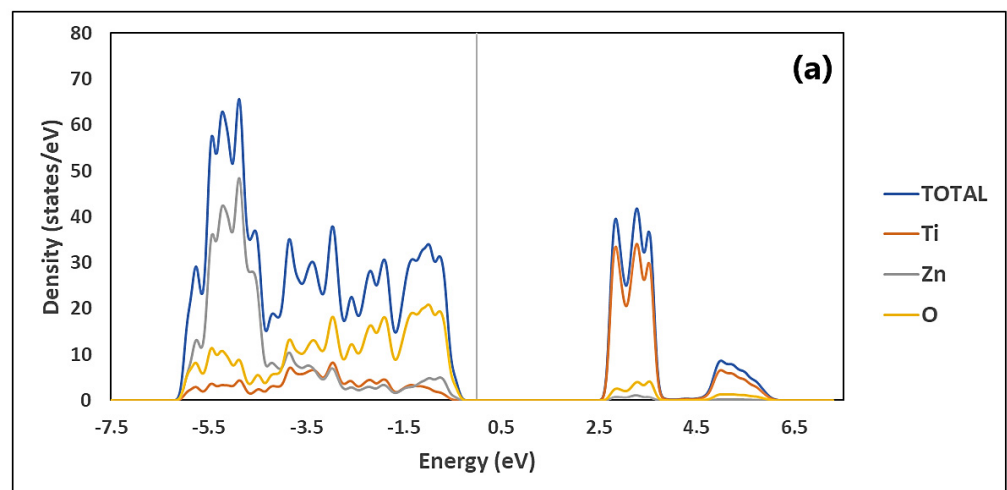


Figure 3. Cont.

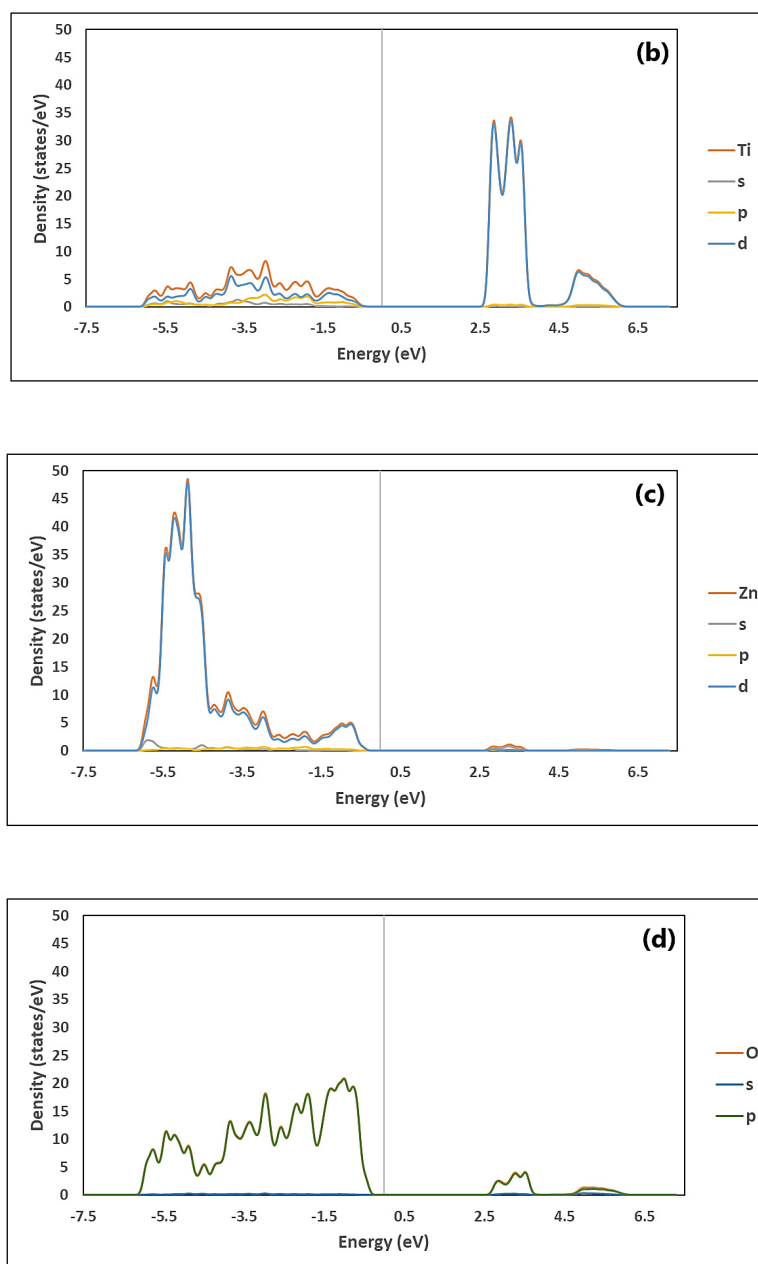


Figure 3. Density of states (DOSs) of ZnTiO_3 : (a) total, and partial: (b) Ti, (c) Zn and (d) O.

In both structures, ZnTiO_3 and TiO_2 , the valence band maximum (VBM) is bordered by the oxygen atom, while the Ti atom determines the conduction band maximum (CBM). Consequently, ZnTiO_3 has an energy bandgap quite similar to that of TiO_2 , due to the fact that ZnTiO_3 involves both ZnO and TiO_2 . Our calculated results agree with the literature [5,18,54].

In order to further understand the chemical bonding of hexagonal ZnTiO_3 and tetragonal TiO_2 , the population analyses were estimated by the Bader method. For ZnTiO_3 , the net charge of Ti ($+2.6e$) was $1.4e$, much smaller than its $+4e$ formal charge, whereas the Zn atom had a positive charge of $+1.4e$ and the O atom had a negative charge of $-1.3e$, which are less than their $+2e$ and $-2e$ formal charges by $0.6e$ and $0.7e$, respectively. For TiO_2 , the net charges of the Ti and O atoms were similar to those calculated for the Ti and O atoms of ZnTiO_3 . These results agree with those reported by other authors [55]. Since the charges on the different bonds can reflect the covalent and ionic properties of the molecule, we concluded that the Ti–O bond is typically covalent for both ZnTiO_3 and TiO_2 and that the

Zn–O bond for ZnTiO₃ is typically ionic; these results coincide with those reported in the literature [42,56].

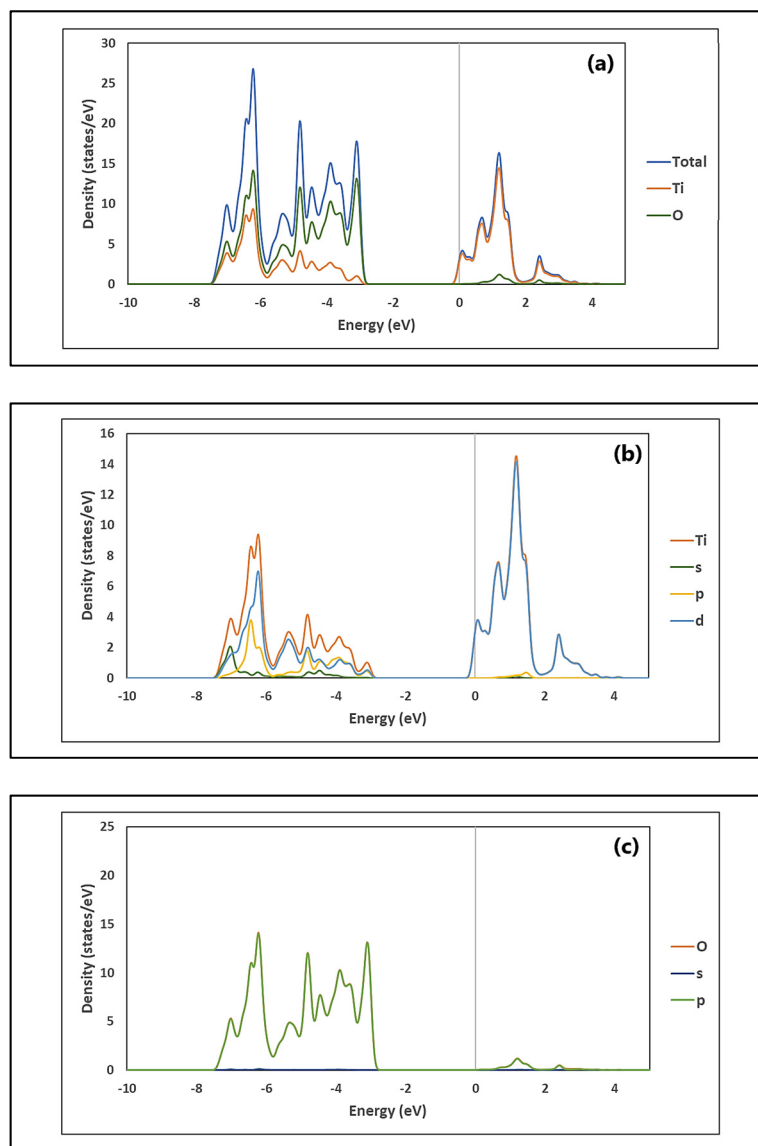


Figure 4. Density of states (DOSs) of TiO₂: (a) total, and partial: (b) Ti and (c) O.

2.2. Adsorption of the MB Dye on the Structures

The orientations of the MB molecule on the ZnTiO₃ and TiO₂ surfaces are shown in Figure 5. Figure 5a shows the horizontal orientation of the MB molecule on the ZnTiO₃ surface, while Figure 5b,c show the semi-perpendicular orientation of the MB molecule on the ZnTiO₃ and TiO₂ surfaces, respectively. The adsorption of the MB molecule on the ZnTiO₃ surface with the molecule placed in semi-perpendicular orientation ($E_{\text{ads}} = -2.916$ eV) was more energetically favored than in the horizontal orientation ($E_{\text{ads}} = -1.310$ eV). Therefore, we studied the adsorption of MB on the TiO₂ surface only with the semi-perpendicular orientation. The calculated adsorption energy for the TiO₂ surface ($E_{\text{ads}} = -0.113$ eV) was less favorable than the calculated adsorption energy for the ZnTiO₃ surface.

The anchoring modes of the MB molecule on the ZnTiO₃ and TiO₂ surfaces are shown in Figure 6. Adsorption of the dye on the ZnTiO₃ and TiO₂ surfaces occurs in a bidentate chelating (BC) adsorption model [57] with two protons oriented toward the nearest surface oxygen [58].

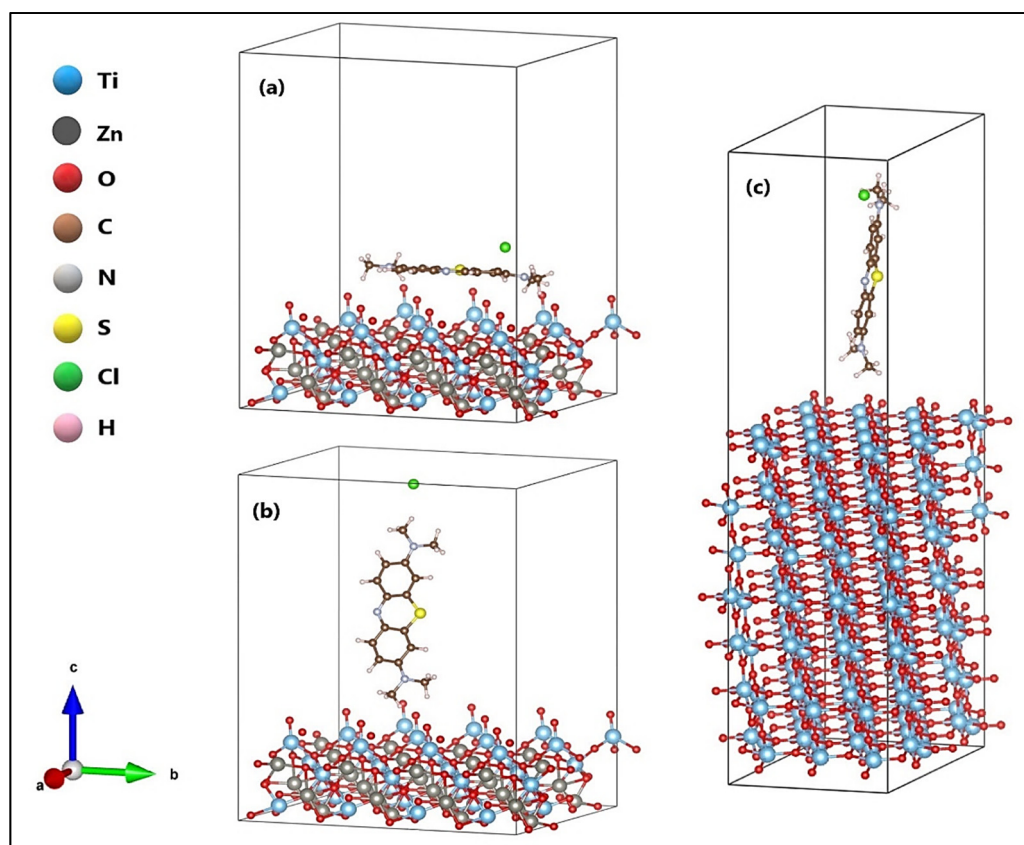


Figure 5. Methylene blue (MB) molecule in (a) horizontal and (b) semi-perpendicular orientation on the ZnTiO₃ surface, and (c) semi-perpendicular orientation on the TiO₂ surfaces.

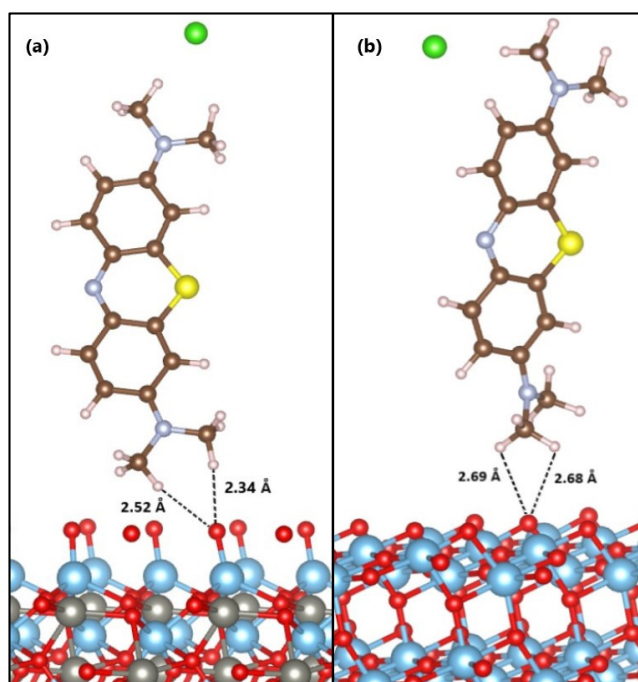


Figure 6. Anchoring modes of the MB molecule on the surface of (a) ZnTiO₃ and (b) TiO₂.

The calculated adsorption energy value indicates that the MB molecule is strongly adsorbed on the ZnTiO₃ surface. The average distances from the hydrogen atoms of the MB molecule (H_{MB}) to the surface plane of ZnTiO₃ are $O_{(oxide)}-H_{MB} = 2.34 \text{ \AA}$ and

$O_{(\text{oxide})}-H_{\text{MB}} = 2.52 \text{ \AA}$. Moreover, the adsorption energy value of the MB molecule on the TiO_2 surface indicates a weaker interaction than on ZnTiO_3 ($E_{\text{ads}} = -0.113 \text{ eV}$). The average distances from the hydrogen atoms of the molecule to the plane of the TiO_2 surface are $O_{(\text{oxide})}-H_{\text{MB}} = 2.68 \text{ \AA}$ and $O_{(\text{oxide})}-H_{\text{MB}} = 2.69 \text{ \AA}$.

3. Discussion

3.1. Optimization and Electronic Structure of ZnTiO_3 and TiO_2

The description of the electronic structure of materials involving transition metals with DFT is often complicated due to correlation effects involving $3d$ electrons [59]. However, since the transition metals of the oxides studied in this paper are formally in the $3d^0$ or $3d^{10}$, neither TiO_2 nor ZnTiO_3 are strongly correlated materials; consequently, a simple DFT approach allowed us to accurately calculate the conduction and valence bands of ZnTiO_3 and TiO_2 .

The literature shows that ZnTiO_3 has a relatively wide bandgap ($E_g = 2.73\text{--}3.70 \text{ eV}$), the value of which depends on the synthesis conditions [60,61]. In our study, the ZnTiO_3 and TiO_2 structures presented indirect bandgap values of 2.20 and 2.31 eV, respectively, which were calculated by the GGA-PBE method. In contrast with the experimental data, 3.18 eV for ZnTiO_3 [15] and 3.20 eV for TiO_2 [53], the theoretical values are lower, and this may be due to the widely known DFT-underestimation of the bandgap in most materials [1,15]. Therefore, a Hubbard U approximation term was adopted to accurately describe the electronic structures [12,62]. The new indirect bandgap values calculated by GGA + U were 3.16 and 3.21 eV for ZnTiO_3 and TiO_2 , respectively, which are consistent with the aforementioned experimental data. As can be seen, mixed oxide ZnTiO_3 has lower bandgap energy than TiO_2 . According to the literature, this occurs due to the replacement of Ti ($3d^0$) atoms with Zn ($3d^{10}$) that induce O $2p$ -Zn $3d^{10}$ repulsion [21,63]. Table 1 shows the comparison of the bandgap energy values of the ZnTiO_3 and TiO_2 calculated in this study with other energy values reported in the literature.

Table 1. Calculated bandgap energy of ZnTiO_3 and TiO_2 and other values reported in the literature.

| Adsorbent | Software Used | Basis Set Used/Functional Used | Bandgap (eV) | Reference |
|------------------|---------------|--------------------------------|--------------|------------|
| ZnTiO_3 | CASTEP | GGA/SP-PBE | 3.14 | [1] |
| ZnTiO_3 | CASTEP | GGA+U | 3.28 | [1] |
| ZnTiO_3 | MS-DMol3 | GGA/PBE | 3.10 | [5] |
| ZnTiO_3 | MS-DMol3 | GGA/PPE-grime | 3.53 | [5] |
| ZnTiO_3 | MS-DMol3 | GGA/PPE-TS | 3.12 | [5] |
| ZnTiO_3 | | Experimental | 3.18 | [15] |
| ZnTiO_3 | VASP | GGA/PBE | 2.96 | [15] |
| ZnTiO_3 | CASTEP | GGA/PW91 | 3.47 | [18] |
| ZnTiO_3 | ABINIT | HSE06 | 4.25 | [56] |
| ZnTiO_3 | ABINIT | GGA/NC | 3.25 | [56] |
| ZnTiO_3 | ABINIT | LDA/NC | 3.05 | [56] |
| ZnTiO_3 | ABINIT | GGA/ultrasoft | 2.96 | [56] |
| ZnTiO_3 | ABINIT | LDA/ultrasoft | 2.86 | [56] |
| ZnTiO_3 | VASP | GGA/PBE+U | 3.16 | This study |
| ZnTiO_3 | VASP | GGA/PBE | 2.20 | This study |
| TiO_2 | VASP | HSE06 | 3.20 | [62] |
| TiO_2 | VASP | GGA/PBE | 2.55 | [58] |
| TiO_2 | VASP | GGA/PBE+U | 3.11 | [58] |
| TiO_2 | | Experimental | 3.20 | [53] |
| TiO_2 | CASTEP | GGA/PBE | 2.70 | [53] |
| TiO_2 | CASTEP | GGA/PBE+U | 3.34 | [53] |
| TiO_2 | ABINIT | GGA/PBE | 2.08 | [64] |
| TiO_2 | ABINIT | GW | 3.71 | [64] |
| TiO_2 | VASP | GGA/PBE | 2.31 | This study |
| TiO_2 | VASP | GGA/PBE+U | 3.21 | This study |

The main character of the electronic structure of ZnTiO_3 originates mainly from the hybridization between the Ti- $3d$ and O- $2p$ states. The Zn- $3d$ and O- $2p$ hybridization and the Ti- $3d$ and O- $2p$ hybridization as well as nonbonding O- $2p$ states are observed at the upper valence bands (VBs). The localized Zn- $3d$ states indicate weak Zn- $3d$ and O- $2p$ hybridization. The states at the lower conduction bands (CBs) are attributed to antibonding states from Ti- $3d$ and O- $2p$. These results agree with those reported by other authors [42]. Similarly, the main character of the electronic structure of TiO_2 originates

from the hybridization between the Ti-3*d* and O-2*p* states. This hybridization, as well as nonbonding O-2*p* states, is observed at the upper valence bands (VBs), while the states at the lower conduction bands (CBs) are attributed to antibonding states from Ti-3*d* and O-2*p*. In both structures, the lowest-energy states are due to the isolated Ti-3*s*, Ti-3*p*, and O-2*s* states. These results also agree with those reported by other authors [5,54,65].

3.2. Adsorption of the MB Dye on the Oxide Models

Several experimental studies of MB removal in aqueous systems have shown that this cationic dye can be easily adsorbed on the ZnTiO₃ and TiO₂ surfaces, due to electrostatic attraction [49]. Therefore, the surface oxygen atoms of both oxides probably generate negatively charged sites that easily attract positive regions of the MB molecule, favoring molecular adsorption.

Our results indicated that the semi-perpendicular orientation of the MB molecule with respect to both oxide surfaces is more favored. In fact, the MB molecule oriented parallel to the surface shows a strong preference for the methyl group of the molecule, while the aromatic ring bends slightly away from the surface due to electrostatic repulsion between the N and S atoms from the aromatic ring and surface oxygen. This is consistent with several studies reporting good adsorption results for dye molecules oriented perpendicular to the adsorbent surface [57,66,67]. Greathouse et al. mentioned that at very high concentrations, this dye forms aggregates that are adsorbed vertically to the surface [68]. Our results suggested that this orientation of the MB molecule on the surface is caused by the balance between electrostatic repulsion between adjacent ions and the strong hydrophobic MB–MB and MB–surface interactions [69].

The MB molecule was adsorbed on the ZnTiO₃ surface (101) with higher negative energy ($E_{\text{ads}} = -2.92$ eV) than on the TiO₂ surface (101) ($E_{\text{ads}} = -0.12$ eV), and the average adsorption distances (O–H) were 2.43 and 2.68 Å for ZnTiO₃ and TiO₂, respectively. According to the optimized configurations, in both cases, the approach is from the two H atoms of the methyl group of the MB molecule to an O atom of each surface. In agreement with the literature, hydrogen bonding can increase the stability of the interaction of a dye with the ZnTiO₃ and TiO₂ surfaces during the adsorption process [70,71]. The Bader charge analysis in Table S1 indicates no significant electronic exchange between the MB molecule and the oxides surface [72]. The results obtained in this theoretical study suggest that MB adsorption is more stable (higher negative adsorption energy) on the ZnTiO₃ surface than on the TiO₂ surface, which is consistent with previous experimental studies.

Pastore et al. suggested three typical coordination schemes: monodentate, bidentate chelating, and bidentate bridging [57]. In our study, we found that the MB molecule is adsorbed on the ZnTiO₃ and TiO₂ surfaces (101) in a bidentate chelating mode, which, according to several authors, produces more stable adsorption with more exothermic adsorption energy [70,73]. The shape of the dye molecules anchored to the oxide significantly affects the molecular adsorption energy. Therefore, calculating the adsorption energy value gives insight into the adherence strength and shape of molecule–surface bonding [66]. The higher the adsorption energy, the higher the retention of the dye on the oxide surface, this being a desirable condition to apply to subsequent photosensitive processes.

In the literature, not enough computational studies of MB adsorption on semiconductors were found; consequently, in Table 2, the results obtained in the present study are compared with those results reported in the literature for the adsorption of other dyes on ZnTiO₃ (101) and TiO₂ (101).

Table 2. Calculated adsorption energy of ZnTiO₃ and TiO₂ and other values reported in the literature.

| Adsorbent | Dye | Software Used | Basis Set/Functional Used | Adsorption | | References |
|--------------------------|-------|---------------|---------------------------|------------|---------|------------|
| | | | | eV | kJ/mol | |
| ZnTiO ₃ (101) | TPA-1 | CASTEP | GGA/PBE | −1.41 | −136.39 | [66] |
| ZnTiO ₃ (101) | TPA-2 | CASTEP | GGA/PBE | −1.63 | −157.47 | [66] |
| ZnTiO ₃ (101) | TPA-3 | CASTEP | GGA/PBE | −5.82 | −561.33 | [66] |

Table 2. Cont.

| Adsorbent | Dye | Software Used | Basis Set/Functional Used | Adsorption | | References |
|-------------------------------|---------|---------------|---------------------------|------------|---------|------------|
| | | | | eV | kJ/mol | |
| ZnTiO ₃ (101) | TPA-4 | CASTEP | GGA/PBE | −2.37 | −228.19 | [66] |
| ZnTiO ₃ (101) (H) | MB | VASP | GGA/PBE | −1.31 | −126.76 | This study |
| ZnTiO ₃ (101) (SP) | MB | VASP | GGA/PBE | −2.92 | −282.05 | This study |
| TiO ₂ (101) | R4-BT | VASP | GGA/PBE | −1.40 | −135.46 | [58] |
| TiO ₂ (101) | R4-F2BT | VASP | GGA/PBE | −1.39 | −134.50 | [58] |
| TiO ₂ (101) | R4-BO | VASP | GGA/PBE | −1.39 | −134.50 | [58] |
| TiO ₂ (101) | R6-Bz | VASP | GGA/PBE | −1.40 | −135.46 | [58] |
| TiO ₂ (101) | R6-BT | VASP | GGA/PBE | −1.38 | −133.53 | [58] |
| TiO ₂ (101) | R6-F2BT | VASP | GGA/PBE | −1.37 | −132.56 | [58] |
| TiO ₂ (101) | R6-BO | VASP | GGA/PBE | −1.37 | −132.56 | [58] |
| TiO ₂ (101) | R6-Bz | VASP | GGA/PBE | −1.38 | −133.53 | [58] |
| TiO ₂ (101) (SP) | MB | VASP | GGA/PBE | −0.12 | −11.61 | This study |

Other research studies should analyze and apply these results to implement adsorptive systems for dyes or similar molecules.

4. Materials and Methods

All Density Functional Theory (DFT) calculations were performed using the Vienna Ab initio Simulation Package (VASP), version 5.3.3 [15,74]. The Perdew–Burke–Ernzerhof (PBE) exchange–correlation functional in the generalized gradient approximation (GGA) proposed by Perdew et al. [75] was employed. The augmented plane wave (PAW) method was used to describe the electron–ion interactions [15]. The cutoff energy to the plane waves was set to 500 eV. The Kohn–Sham equations [76,77] were solved self-consistently until the energy variation between cycles was less than 10^{-5} eV. The first Brillouin zone was sampled using Monkhorst–Pack [78] *k*-point meshes to calculate the bulk properties of ZnTiO₃ and TiO₂, in particular, $3 \times 7 \times 5$ and $3 \times 3 \times 1$, respectively. All atomic positions were fully relaxed until the forces on each atom were below 0.01 eV/Å. The computational parameters were selected seeking the best balance between computational cost and precision. The tested values were as follows: energy cutoff points = 450, 475, 500, and 515 eV; force convergence criterion for ionic relaxation = 0.08, 0.04, 0.02, 0.01, and 0.005 eV/Å and number of *k*-points corresponding to *k*-spacing in each axe = 0.35, 0.30, 0.25, 0.20, and 0.15. The parameters were optimized until the difference between the energy values of the system was lower than 10^{-4} eV.

The Gaussian smearing method with $\sigma = 0.10$ eV was applied to band occupations in order to improve total energy convergence [15]. A Hubbard *U* approximation term was adopted to describe the strong on-site Coulomb repulsion in order to accurately explain the electronic structures [62], which is not correctly described by the PBE functional [58]. Population analyses were estimated using Bader’s charge analysis code, which provided important information on bonding behaviors from the atomic charge values [79–81]. All calculations were non-spin polarized and all molecular models were created and visualized using BioVia Material Studio, version 5.5.

To study MB adsorption, an optimized molecular structure was used [68]. The bulk of both ZnTiO₃ and TiO₂ crystals was cleaved on the surface (101), since it is the most stable surface according to the literature [54,57,62,66,82]. The slab model of ZnTiO₃ (101) was a supercell $p(2 \times 3)$ with three atomic layers, which includes 36 Zn atoms, 36 Ti atoms, and 108 O atoms. On the other hand, the TiO₂ (101) surface model has seven atomic layers with a $p(3 \times 3)$ structure of the original unit cell, which includes 168 Ti atoms and 336 O atoms.

An appropriate vacuum thickness of each structure was chosen by calculating the surface energy. For both ZnTiO₃ and TiO₂ surface models, a vacuum of 20 Å was added. The surface energies (γ_s) were calculated using the following equation [83]:

$$\gamma_s = \frac{(E_{slab} - n \times E_{bulk})}{2A} \quad (1)$$

where E_{slab} is the total energy of the slab material (eV), E_{bulk} is the total energy of the bulk material (eV), n is the number of atoms contained in the slab, and A is the surface area (Å²). The values for the surface energies (γ_s) of the ZnTiO₃ and TiO₂ structures with a vacuum distance of 20 Å were 0.076 eV/Å² (7.30 kJ/Å²) and 0.062 eV/Å² (5.98 kJ/Å²), respectively.

Adsorption calculation was initiated with the MB molecule placed close to the surface of each oxide in at least one of the following orientations, horizontal (H) and semi-perpendicular (SP), with respect to the surface.

The adsorption energy (ΔE_{ads}) of the MB molecule on the surface of both ZnTiO₃ and TiO₂ oxides was calculated using the following equation [84]:

$$\Delta E_{ads} = E_{MB/oxide} - E_{oxide} - E_{MB} \quad (2)$$

where $E_{MB/oxide}$ is the energy of the supersystem formed by the adsorbed molecule on the surface (eV), E_{oxide} is the energy of the clean oxide (eV), and E_{MB} is the energy of the isolated molecule in vacuum (eV).

5. Conclusions

The aim of this comparative study was to use molecular simulation to address unresolved issues related to the adsorption mechanism of methylene blue on both ZnTiO₃ and TiO₂. DFT calculations of MB adsorption on the surface (101) of both ZnTiO₃ and TiO₂ indicated that adsorption on ZnTiO₃ was stronger than on TiO₂. The semi-perpendicular orientation was the most probable molecular approach to the oxide surfaces. Electrostatic repulsion due to the proximity of adjacent S and N atoms when MB was in high concentration was overcome by the much stronger interactions between the methyl groups and the surface oxygen atoms of ZnTiO₃ and TiO₂.

Finally, we computationally corroborated the feasibility of using ZnTiO₃ as an MB adsorbent material, as experimentally found. Theoretically, we forecast the appealing prospect for this material according to the adsorption energy and the large bandgap calculated by DFT, which is in addition to the experimental results that we reported in a previous paper. Our study verifies that ZnTiO₃ has better MB adsorption energy than TiO₂ in the anatase phase, which is important to enhance a subsequent degradation process. The large bandgap obtained by DFT calculations also shows that ZnTiO₃ can potentially be used as a photocatalyst, allowing for complete degradation of the dye after being adsorbed. Therefore, considering only the band structure, ZnTiO₃ fully meets the necessary requirements to be a photocatalyst. As already mentioned, however, in addition to the band structure, the adsorption capacity is also very important for photocatalytic materials. In this way, ZnTiO₃ constitutes an efficient alternative material for various technological and environmental applications.

Supplementary Materials: The following are available online. Figure S1: Aromatic ring of MB bent slightly on the ZnTiO₃ surface (101); Figure S2: Optimization energies of ZnTiO₃, TiO₂ and MB; Table S1: Coordinates of the optimized structures; Table S2: Bader's charge analysis of the methylene blue molecule.

Author Contributions: Conceptualization, S.G. and X.J.-F.; methodology, S.G., X.J.-F. and L.F.C.; software, S.G. and X.J.-F.; validation, F.M., S.G. and X.J.-F.; formal analysis, S.G. and X.J.-F.; investigation, S.G., X.J.-F. and L.F.C.; resources, S.G. and F.M.; data curation, S.G. and X.J.-F.; writing—original draft preparation, X.J.-F.; writing—review and editing, S.G., F.M. and X.J.-F.; supervision, S.G. and F.M. All authors have read and agreed to the published version of the manuscript.

Funding: This research received no external funding.

Institutional Review Board Statement: Not applicable.

Informed Consent Statement: Not applicable.

Data Availability Statement: Data are contained within the article and Supplementary Materials.

Acknowledgments: The authors would like to thank Henry Quezada for the computer support. This paper was financially supported by Universitat Rovira I Virgili (Spain) and Universidad Técnica Particular de Loja (Ecuador).

Conflicts of Interest: The authors declare no conflict of interest.

Sample Availability: Samples of the compounds are not available from the authors.

References

1. Obodo, K.O.; Noto, L.L.; Mofokeng, S.J.; Ouma, C.N.M.; Braun, M.; Dhlamini, M.S. Influence of Tm, Ho and Er dopants on the properties of Yb activated ZnTiO₃ perovskite: A density functional theory insight. *Mater. Res. Express* **2018**, *5*. [[CrossRef](#)]
2. Li, L.; Zhang, X.; Zhang, W.; Wang, L.; Chen, X.; Gao, Y. Microwave-assisted synthesis of nanocomposite Ag/ZnO-TiO₂ and photocatalytic degradation Rhodamine B with different modes. *Colloids Surf. A Physicochem. Eng. Asp.* **2014**, *457*, 134–141. [[CrossRef](#)]
3. Ozturk, B.; Soyulu, G.S.P. Promoting role of transition metal oxide on ZnTiO₃-TiO₂ nanocomposites for the photocatalytic activity under solar light irradiation. *Ceram. Int.* **2016**, *42*, 11184–11192. [[CrossRef](#)]
4. Grabis, J.; Letlena, A.; Sipiola, I. Preparation and properties of photocatalysts in ZnO/TiO₂ system. *Key Eng. Mater.* **2019**, *800*, 170–174. [[CrossRef](#)]
5. Cherifi, K.; Cheknane, A.; Benghia, A.; Hilal, H.S.; Rahmoun, K.; Benyoucef, B.; Goumri-Said, S. Exploring N3 ruthenium dye adsorption onto ZnTiO₃ (101) and (110) surfaces for dye sensitized solar cell applications: Full computational study. *Mater. Today Energy* **2019**, *13*, 109–118. [[CrossRef](#)]
6. Lee, C.-G.; Na, K.-H.; Kim, W.-T.; Park, D.-C.; Yang, W.-H.; Choi, W.-Y. TiO₂/ZnO nanofibers prepared by electrospinning and their photocatalytic degradation of methylene blue compared with TiO₂ nanofibers. *Appl. Sci.* **2019**, *9*, 3404. [[CrossRef](#)]
7. Irani, M.; Mohammadi, T.; Mohebbi, S. Photocatalytic degradation of methylene blue with zno nanoparticles; a joint experimental and theoretical study. *J. Mex. Chem. Soc.* **2017**, *60*, 218–225. [[CrossRef](#)]
8. Sinha, D.; De, D.; Goswami, D.; Mondal, A.; Ayaz, A. ZnO and TiO₂ nanostructured dye sensitized solar photovoltaic cell. *Mater. Today Proc.* **2019**, *11*, 782–788. [[CrossRef](#)]
9. Ranjith, K.S.; Uyar, T. ZnO-TiO₂ composites and ternary ZnTiO₃ electrospun nanofibers: The influence of annealing on the photocatalytic response and reusable functionality. *CrystEngComm* **2018**, *20*, 5801–5813. [[CrossRef](#)]
10. Chen, F.; Yu, C.; Wei, L.; Fan, Q.; Ma, F.; Zeng, J.; Yi, J.; Yang, K.; Ji, H. Fabrication and characterization of ZnTiO₃/Zn₂Ti₃O₈/ZnO ternary photocatalyst for synergetic removal of aqueous organic pollutants and Cr(VI) ions. *Sci. Total Environ.* **2020**, *706*, 136026. [[CrossRef](#)]
11. Zalani, N.M.; Kaleji, B.K.; Mazinani, B. Synthesis and characterisation of the mesoporous ZnO-TiO₂ nanocomposite; Taguchi optimisation and photocatalytic methylene blue degradation under visible light. *Mater. Technol.* **2019**, *35*, 281–289. [[CrossRef](#)]
12. Dutta, D.P.; Singh, A.; Tyagi, A. Ag doped and Ag dispersed nano ZnTiO₃: Improved photocatalytic organic pollutant degradation under solar irradiation and antibacterial activity. *J. Environ. Chem. Eng.* **2014**, *2*, 2177–2187. [[CrossRef](#)]
13. Fu, R.; Wang, Q.; Gao, S.; Wang, Z.; Huang, B.; Dai, Y.; Lu, J. Effect of different processes and Ti/Zn molar ratios on the structure, morphology, and enhanced photoelectrochemical and photocatalytic performance of Ti³⁺ self-doped titanium-zinc hybrid oxides. *J. Power Sources* **2015**, *285*, 449–459. [[CrossRef](#)]
14. Li, X.; Xiong, J.; Huang, J.; Feng, Z.; Luo, J. Novel g-C₃N₄/h'ZnTiO₃-a'/TiO₂ direct Z-scheme heterojunction with significantly enhanced visible-light photocatalytic activity. *J. Alloys Compd.* **2019**, *774*, 768–778. [[CrossRef](#)]
15. Yu, J.; Li, N.; Zhu, L.; Xu, X. Application of ZnTiO₃ in quantum-dot-sensitized solar cells and numerical simulations using first-principles theory. *J. Alloys Compd.* **2016**, *681*, 88–95. [[CrossRef](#)]
16. Sarkar, M.; Sarkar, S.; Biswas, A.; De, S.; Kumar, P.R.; Mothi, E.M.; Kathiravan, A. Zinc titanate nanomaterials—Photocatalytic studies and sensitization of hydantoin derivatized porphyrin dye. *Nano-Struct. Nano-Objects* **2020**, *21*, 100412. [[CrossRef](#)]
17. Baamran, K.S.; Tahir, M. Ni-embedded TiO₂-ZnTiO₃ reducible perovskite composite with synergistic effect of metal/support towards enhanced H₂ production via phenol steam reforming. *Energy Convers. Manag.* **2019**, *200*, 112064. [[CrossRef](#)]
18. Liu, Q.-J.; Zhang, N.-C.; Liu, F.-S.; Wang, H.-Y.; Liu, Z.-T. Theoretical study of structural, elastic, electronic properties, and dispersion of optical functions of hexagonal ZnTiO₃. *Phys. Status Solidi Basic Res.* **2013**, *250*, 1810–1815. [[CrossRef](#)]
19. Yan, X.; Zhao, C.-L.; Zhou, Y.-L.; Wu, Z.-J.; Yuan, J.-M.; Li, W.-S. Synthesis and characterization of ZnTiO₃ with high photocatalytic activity. *Trans. Nonferrous Met. Soc. China Engl. Ed.* **2015**, *25*, 2272–2278. [[CrossRef](#)]
20. Li, M.; Jiao, B. Synthesis and photoluminescence properties of ZnTiO₃:Eu³⁺ red phosphors via sol-gel method. *J. Rare Earths* **2015**, *33*, 231–238. [[CrossRef](#)]

21. Lv, J.; Tang, M.; Quan, R.; Chai, Z. Synthesis of solar heat-reflective ZnTiO₃ pigments with novel roof cooling effect. *Ceram. Int.* **2019**, *45*, 15768–15771. [[CrossRef](#)]
22. Sowmyashree, A.; Somya, A.; Kumar, C.P.; Rao, S. Novel nano corrosion inhibitor, integrated zinc titanate nano particles: Synthesis, characterization, thermodynamic and electrochemical studies. *Surf. Interfaces* **2021**, *22*, 100812. [[CrossRef](#)]
23. Tavakoli-Azar, T.; Mahjoub, A.R.; Sadjadi, M.S.; Farhadyar, N.; Sadr, M.H. Improving the photocatalytic performance of a perovskite ZnTiO₃ through ZnTiO₃@S nanocomposites for degradation of Crystal violet and Rhodamine B pollutants under sunlight. *Inorg. Chem. Commun.* **2020**, *119*, 108091. [[CrossRef](#)]
24. Raveendra, R.; Prashanth, P.; Krishna, R.H.; Bhagya, N.; Nagabhushana, B.; Naika, H.R.; Lingaraju, K.; Nagabhushana, H.; Prasad, B.D. Synthesis, structural characterization of nano ZnTiO₃ ceramic: An effective azo dye adsorbent and antibacterial agent. *J. Asian Ceram. Soc.* **2014**, *2*, 357–365. [[CrossRef](#)]
25. Kurajica, S.; Minga, I.; Blazic, R.; Muzina, K.; Tominac, P. Adsorption and degradation kinetics of methylene blue on as-prepared and calcined titanate nanotubes. *Athens J. Sci.* **2018**, *5*, 7–22. [[CrossRef](#)]
26. Sahu, A.; Chaurasiya, R.; Hiremath, K.; Dixit, A. Nanostructured zinc titanate wide band gap semiconductor as a photoelectrode material for quantum dot sensitized solar cells. *Sol. Energy* **2018**, *163*, 338–346. [[CrossRef](#)]
27. Inaguma, Y.; Aimi, A.; Shirako, Y.; Sakurai, D.; Mori, D.; Kojitani, H.; Akaogi, M.; Nakayama, M. High-pressure synthesis, crystal structure, and phase stability relations of a LiNbO₃-type polar titanate ZnTiO₃ and its reinforced polarity by the second-order Jahn-Teller effect. *J. Am. Chem. Soc.* **2013**, *136*, 2748–2756. [[CrossRef](#)]
28. Ruiz-Fuertes, J.; Winkler, B.; Bernert, T.; Bayarjargal, L.; Morgenroth, W.; Koch-Müller, M.; Refson, K.; Milman, V.; Tamura, N. Ferroelectric soft mode of polar ZnTiO₃ investigated by Raman spectroscopy at high pressure. *Phys. Rev. B Condens. Matter Mater. Phys.* **2015**, *91*, 214110. [[CrossRef](#)]
29. Pawar, R.C.; Kang, S.; Park, J.H.; Kim, J.-H.; Ahn, S.; Lee, C.S. Evaluation of a multi-dimensional hybrid photocatalyst for enrichment of H₂ evolution and elimination of dye/non-dye pollutants. *Catal. Sci. Technol.* **2017**, *7*, 2579–2590. [[CrossRef](#)]
30. Salavati-Niasari, M.; Soofivand, F.; Sobhani-Nasab, A.; Shakouri-Arani, M.; Faal, A.Y.; Bagheri, S. Synthesis, characterization, and morphological control of ZnTiO₃ nanoparticles through sol-gel processes and its photocatalyst application. *Adv. Powder Technol.* **2016**, *27*, 2066–2075. [[CrossRef](#)]
31. Ke, S.; Cheng, X.; Wang, Q.; Wang, Y.; Pan, Z. Preparation of a photocatalytic TiO₂/ZnTiO₃ coating on glazed ceramic tiles. *Ceram. Int.* **2014**, *40*, 8891–8895. [[CrossRef](#)]
32. Acosta-Silva, Y.D.J.; Castanedo-Perez, R.; Torres-Delgado, G.; Méndez-López, A.; Zelaya-Angel, O. Analysis of the photocatalytic activity of CdS+ZnTiO₃ nanocomposite films prepared by sputtering process. *Superlattices Microstruct.* **2016**, *100*, 148–157. [[CrossRef](#)]
33. Yadav, B.; Yadav, A.; Singh, S.; Singh, K. Nanocrystalline zinc titanate synthesized via physicochemical route and its application as liquefied petroleum gas sensor. *Sens. Actuators B Chem.* **2013**, *177*, 605–611. [[CrossRef](#)]
34. Tahay, P.; Khani, Y.; Jabari, M.; Bahadoran, F.; Safari, N.; Zamanian, A. Synthesis of cubic and hexagonal ZnTiO₃ as catalyst support in steam reforming of methanol: Study of physical and chemical properties of copper catalysts on the H₂ and CO selectivity and coke formation. *Int. J. Hydrog. Energy* **2020**, *45*, 9484–9495. [[CrossRef](#)]
35. Edalatfar, M.; Yazdani, F.; Salehi, M.B. Synthesis and identification of ZnTiO₃ nanoparticles as a rheology modifier additive in water-based drilling mud. *J. Pet. Sci. Eng.* **2021**, *201*, 108415. [[CrossRef](#)]
36. Bhagwat, U.O.; Wu, J.J.; Asiri, A.M.; Anandan, S. Synthesis of ZnTiO₃@TiO₂ heterostructure nanomaterial as a visible light photocatalyst. *ChemistrySelect* **2019**, *4*, 6106–6112. [[CrossRef](#)]
37. Lei, S.; Fan, H.; Ren, X.; Fang, J.; Ma, L.; Liu, Z. Novel sintering and band gap engineering of ZnTiO₃ ceramics with excellent microwave dielectric properties. *J. Mater. Chem. C* **2017**, *5*, 4040–4047. [[CrossRef](#)]
38. Pantoja-Espinoza, J.C.; Domínguez-Arvizu, J.L.; Jiménez-Miramontes, J.A.; Hernández-Majalca, B.C.; Meléndez-Zaragoza, M.J.; Salinas-Gutiérrez, J.M.; Herrera-Pérez, G.M.; Collins-Martínez, V.H.; López-Ortiz, A. Comparative study of Zn₂Ti₃O₈ and ZnTiO₃ photocatalytic properties for hydrogen production. *Catalysts* **2020**, *10*, 1372. [[CrossRef](#)]
39. Jaramillo-Fierro, X.; Pérez, S.G.; Jaramillo, X.; Cabello, F.M. Synthesis of the ZnTiO₃/TiO₂ nanocomposite supported in ecuadorian clays for the adsorption and photocatalytic removal of methylene blue dye. *Nanomaterials* **2020**, *10*, 1891. [[CrossRef](#)]
40. Jaramillo-Fierro, X.; González, S.; Montesdeoca-Mendoza, F.; Medina, F. Structuring of zntio₃/tio₂ adsorbents for the removal of methylene blue, using zeolite precursor clays as natural additives. *Nanomaterials* **2021**, *11*, 898. [[CrossRef](#)]
41. Zhang, Z.; Yates, J.J.T. Band bending in semiconductors: Chemical and physical consequences at surfaces and interfaces. *Chem. Rev.* **2012**, *112*, 5520–5551. [[CrossRef](#)] [[PubMed](#)]
42. Xiao-Chao, Z.; Cai-Mei, F.; Zhen-Hai, L.; Pei-De, H. Electronic structures and optical properties of ilmenite-type hexagonal ZnTiO₃. *Wuli Huaxue Xuebao/Acta Phys. Chim. Sin.* **2011**, *27*, 47–51. [[CrossRef](#)]
43. Conesa, J.C. Band structures and nitrogen doping effects in zinc titanate photocatalysts. *Catal. Today* **2013**, *208*, 11–18. [[CrossRef](#)]
44. Gil, A.; Assis, F.; Albeniz, S.; Korili, S. Removal of dyes from wastewaters by adsorption on pillared clays. *Chem. Eng. J.* **2011**, *168*, 1032–1040. [[CrossRef](#)]
45. Laysandra, L.; Sari, M.W.M.K.; Soetaredjo, F.E.; Foe, K.; Putro, J.N.; Kurniawan, A.; Ju, Y.-H.; Ismadji, S. Adsorption and photocatalytic performance of bentonite-titanium dioxide composites for methylene blue and rhodamine B decoloration. *Heliyon* **2017**, *3*, e00488. [[CrossRef](#)]

46. Mehrabi, M.; Javanbakht, V. Photocatalytic degradation of cationic and anionic dyes by a novel nanophotocatalyst of $\text{TiO}_2/\text{ZnTiO}_3/\alpha\text{Fe}_2\text{O}_3$ by ultraviolet light irradiation. *J. Mater. Sci. Mater. Electron.* **2018**, *29*, 9908–9919. [[CrossRef](#)]
47. Subramaniam, M.N.; Goh, P.S.; Abdullah, N.; Lau, W.J.; Ng, B.C.; Ismail, A.F. Adsorption and photocatalytic degradation of methylene blue using high surface area titanate nanotubes (TNT) synthesized via hydrothermal method. *J. Nanoparticle Res.* **2017**, *19*, 220. [[CrossRef](#)]
48. Abdellah, M.; Nosier, S.; El-Shazly, A.; Mubarak, A. Photocatalytic decolorization of methylene blue using TiO_2/UV system enhanced by air sparging. *Alex. Eng. J.* **2018**, *57*, 3727–3735. [[CrossRef](#)]
49. Sutanto, N.; Saharudin, K.A.; Sreekantan, S.; Kumaravel, V.; Akil, H.M. Heterojunction catalysts $\text{g-C}_3\text{N}_4/-3\text{ZnO-c-Zn}_2\text{Ti}_3\text{O}_8$ with highly enhanced visible-light-driven photocatalytic activity. *J. Sol-Gel Sci. Technol.* **2020**, *93*, 354–370. [[CrossRef](#)]
50. Zhao, Q.; Zhang, L.; Wang, X.; Jia, X.; Xu, P.; Zhao, M.; Dai, R. Simultaneous efficient adsorption and photocatalytic degradation of methylene blue over iron(III)-based metal–organic frameworks: A comparative study. *Transit. Met. Chem.* **2019**, *44*, 789–797. [[CrossRef](#)]
51. Chang-Guo, Z. Development and application of first-principles electronic structure approach for molecules in solution based on fully polarizable continuum model. *Wuli Huaxue Xuebao/Acta Phys. Chim. Sin.* **2011**, *27*, 1–10. [[CrossRef](#)]
52. Hinuma, Y.; Pizzi, G.; Kumagai, Y.; Oba, F.; Tanaka, I. Band structure diagram paths based on crystallography. *Comput. Mater. Sci.* **2017**, *128*, 140–184. [[CrossRef](#)]
53. Zhang, R.; Zhao, J.; Yang, Y.; Lu, Z.; Shi, W. Understanding electronic and optical properties of La and Mn co-doped anatase TiO_2 . *Comput. Condens. Matter* **2016**, *6*, 5–17. [[CrossRef](#)]
54. Qi, K.; Selvaraj, R.; Al Fahdi, T.; Al-Kindy, S.; Kim, Y.; Wang, G.-C.; Tai, C.-W.; Sillanpää, M. Enhanced photocatalytic activity of anatase- TiO_2 nanoparticles by fullerene modification: A theoretical and experimental study. *Appl. Surf. Sci.* **2016**, *387*, 750–758. [[CrossRef](#)]
55. Koch, D.; Golub, P.; Manzhos, S. Stability of charges in titanium compounds and charge transfer to oxygen in titanium dioxide. *J. Phys. Conf. Ser.* **2018**, *1136*, 012017. [[CrossRef](#)]
56. Zhang, J.; Xu, B.; Wang, Y.-S.; Qin, Z.; Ke, S.-H. First-principles investigation of the ferroelectric, piezoelectric and nonlinear optical properties of LiNbO_3 -type ZnTiO_3 . *Sci. Rep.* **2019**, *9*, 1–14. [[CrossRef](#)]
57. Pastore, M.; De Angelis, F. Computational modelling of TiO_2 surfaces sensitized by organic dyes with different anchoring groups: Adsorption modes, electronic structure and implication for electron injection/recombination. *Phys. Chem. Chem. Phys.* **2012**, *14*, 920–928. [[CrossRef](#)]
58. Samanta, P.K.; English, N.J. Opto-electronic properties of stable blue photosensitisers on a TiO_2 anatase-101 surface for efficient dye-sensitized solar cells. *Chem. Phys. Lett.* **2019**, *731*, 136624. [[CrossRef](#)]
59. Cramer, C.J.; Truhlar, D. Density functional theory for transition metals and transition metal chemistry. *Phys. Chem. Chem. Phys.* **2009**, *11*, 10757–10816. [[CrossRef](#)]
60. Wang, J.; Wang, D.; Zhang, X.; Zhao, C.; Zhang, M.; Zhang, Z.; Wang, J. An anti-symmetric dual (ASD) Z-scheme photocatalytic system: $(\text{ZnIn}_2\text{S}_4/\text{Er}^{3+}:\text{Y}_3\text{Al}_5\text{O}_{12})@(\text{ZnTiO}_3/\text{CaIn}_2\text{S}_4)$ for organic pollutants degradation with simultaneous hydrogen evolution. *Int. J. Hydrogen Energy* **2019**, *44*, 6592–6607. [[CrossRef](#)]
61. Wang, Y.-W.; Yuan, P.-H.; Fan, C.-M.; Wang, Y.; Ding, G.-Y.; Wang, Y.-F. Preparation of zinc titanate nanoparticles and their photocatalytic behaviors in the photodegradation of humic acid in water. *Ceram. Int.* **2012**, *38*, 4173–4180. [[CrossRef](#)]
62. Khan, S.; Cho, H.; Kim, D.; Han, S.S.; Lee, K.H.; Cho, S.-H.; Song, T.; Choi, H. Defect engineering toward strong photocatalysis of Nb-doped anatase TiO_2 : Computational predictions and experimental verifications. *Appl. Catal. B Environ.* **2017**, *206*, 520–530. [[CrossRef](#)]
63. McLeod, J.A.; Moewes, A.; Zatssepina, D.A.; Kurmaev, E.Z.; Wypych-Puszkarski, A.; Bobowska, I.; Opasinska, A.; Cholakh, S.O. Predicting the band gap of ternary oxides containing 3d10 and 3d0 metals. *Phys. Rev. B Condens. Matter Mater. Phys.* **2012**, *86*, 195207. [[CrossRef](#)]
64. Zhu, T.; Gao, S.-P. The stability, electronic structure, and optical property of TiO_2 polymorphs. *J. Phys. Chem. C* **2014**, *118*, 11385–11396. [[CrossRef](#)]
65. Hossain, F.M.; Evteev, A.V.; Belova, I.V.; Nowotny, J.; Murch, G.E. First-principles calculations of a corrugated anatase TiO_2 surface. *Comput. Mater. Sci.* **2012**, *51*, 78–82. [[CrossRef](#)]
66. Cherifi, K.; Cheknane, A.; Hilal, H.S.; Benghia, A.; Rahmoun, K.; Benyoucef, B. Investigation of triphenylamine-based sensitizer characteristics and adsorption behavior onto ZnTiO_3 perovskite (1 0 1) surfaces for dye-sensitized solar cells using first-principle calculation. *Chem. Phys.* **2020**, *530*, 110595. [[CrossRef](#)]
67. Zhu, H.-C.; Li, C.-F.; Fu, Z.-H.; Wei, S.-S.; Zhu, X.-F.; Zhang, J. Increasing the open-circuit voltage and adsorption stability of squaraine dye binding onto the TiO_2 anatase (1 0 1) surface via heterocyclic anchoring groups used for DSSC. *Appl. Surf. Sci.* **2018**, *455*, 1095–1105. [[CrossRef](#)]
68. Greathouse, J.A.; Geatches, D.L.; Pike, D.Q.; Greenwell, H.; Johnston, C.T.; Wilcox, J.; Cygan, R.T. Methylene blue adsorption on the basal surfaces of kaolinite: Structure and thermodynamics from quantum and classical molecular simulation. *Clays Clay Miner.* **2015**, *63*, 185–198. [[CrossRef](#)]
69. Zhong, L.; Hu, Y.; Xing, D. Adsorption orientation of methylene blue (MB+) on the silver colloid: SERS and DFT studies. In Proceedings of the 2009 Conference on Lasers & Electro Optics & The Pacific Rim Conference on Lasers and Electro-Optics, Shanghai, China, 30 August–3 September 2009; pp. 1–2. [[CrossRef](#)]

70. Orellana, W. D- π -A dye attached on TiO₂(101) and TiO₂(001) surfaces: Electron transfer properties from ab initio calculations. *Sol. Energy* **2021**, *216*, 266–273. [[CrossRef](#)]
71. Qin, H.-C.; Qin, Q.-Q.; Luo, H.; Wei, W.; Liu, L.-X.; Li, L.-C. Theoretical study on adsorption characteristics and environmental effects of dimetridazole on TiO₂ surface. *Comput. Theor. Chem.* **2019**, *1150*, 10–17. [[CrossRef](#)]
72. Kuganathan, N.; Chroneos, A. Hydrogen adsorption on Ru-encapsulated, -doped and -supported surfaces of C60. *Surfaces* **2020**, *3*, 30. [[CrossRef](#)]
73. Mathew, S.; Yella, A.; Gao, P.; Humphry-Baker, R.; Curchod, B.F.E.; Ashari-Astani, N.; Tavernelli, I.; Rothlisberger, U.; Nazeeruddin, K.; Graetzel, M. Dye-sensitized solar cells with 13% efficiency achieved through the molecular engineering of porphyrin sensitizers. *Nat. Chem.* **2014**, *6*, 242–247. [[CrossRef](#)]
74. Kresse, G.; Furthmüller, J. Efficient iterative schemes for ab initio total-energy calculations using a plane-wave basis set. *Phys. Rev. B Condens. Matter Mater. Phys.* **1996**, *54*, 11169–11186. [[CrossRef](#)]
75. Perdew, J.P.; Burke, K.; Ernzerhof, M. Generalized gradient approximation made simple. *Phys. Rev. Lett.* **1996**, *77*, 3865–3868. [[CrossRef](#)]
76. Kohn, W.; Sham, L. Quantum density oscillations in an inhomogeneous electron gas. *Phys. Rev.* **1965**, *137*, A1697–A1705. [[CrossRef](#)]
77. Wang, Y.A.; Xiang, P. From the Hohenberg-Kohn theory to the Kohn-Sham equations. In *Recent Progress in Orbital-free Density Functional Theory*; World Scientific: Singapore, 2013; pp. 3–12.
78. Monkhorst, H.J.; Pack, J.D. Special points for Brillouin-zone integrations. *Phys. Rev. B* **1976**, *13*, 5188–5192. [[CrossRef](#)]
79. Voityuk, A.A.; Stasyuk, A.J.; Vyboishchikov, S.F. A simple model for calculating atomic charges in molecules. *Phys. Chem. Chem. Phys.* **2018**, *20*, 23328–23337. [[CrossRef](#)]
80. Yu, M.; Trinkle, D.R. Accurate and efficient algorithm for Bader charge integration. *J. Chem. Phys.* **2011**, *134*, 064111. [[CrossRef](#)]
81. Kumar, P.S.V.; Raghavendra, V.; Subramanian, V. Bader's Theory of Atoms in Molecules (AIM) and its Applications to Chemical Bonding. *J. Chem. Sci.* **2016**, *128*, 1527–1536. [[CrossRef](#)]
82. Martinez, J.; Sinnott, S.B.; Phillpot, S.R. Adhesion and diffusion at TiN/TiO₂ interfaces: A first principles study. *Comput. Mater. Sci.* **2017**, *130*, 249–256. [[CrossRef](#)]
83. German, E.; Faccio, R.; Mombrú, A.W. Comparison of standard DFT and Hubbard-DFT methods in structural and electronic properties of TiO₂ polymorphs and H-titanate ultrathin sheets for DSSC application. *Appl. Surf. Sci.* **2018**, *428*, 118–123. [[CrossRef](#)]
84. Pillai, R.S.; Khan, I.; Titus, E. C₂-Hydrocarbon Adsorption in Nano-porous Faujasite: A DFT Study. *Mater. Today Proc.* **2015**, *2*, 436–445. [[CrossRef](#)]